

Towards Active Rotor Analysis using Viscous Vortex Particle Method

Sumeet Kumar

PhD Candidate

Institute of Helicopter Technology and VTOL

Technical University of Munich

Munich, Germany

Juergen Rauleder

Assistant Professor

Daniel Guggenheim School of Aerospace Engineering

Georgia Institute of Technology

Atlanta, GA, USA

Ilkay Yavrucuk

Professor

Institute of Helicopter Technology and VTOL

Technical University of Munich

Munich, Germany

ABSTRACT

This study explores the potential of the incompressible viscous vortex particle method (VVPM) formulation to model the unsteady rotor wake effects on blade aerodynamic loads. Preliminary validation results have been presented verifying the VVPM formulation. The particle method is coupled with a comprehensive rotor aeromechanical analysis code Dymore in order to improve the rotor wake modelling capability of the overall rotor analysis setup. The coupled Dymore+VVPM framework was verified by using static as well as dynamic wing cases in order to assess the ability of VVPM to accurately model wake induced velocities. The current study is the first step towards active rotor analysis using this coupled framework. Consequently, the ability of VVPM to capture unsteady aerodynamic effects due to wing pitching as well as active morphing was tested.

INTRODUCTION

Modelling active rotor systems in some form has been in pursuit for more than half a century. The research in this field started with higher harmonic actuation of the rotor swashplate in the stationary frame. Since then, both computational and experimental investigations have focused on accurately assessing the performance, acoustics and vibration improvement possible through the use of active mechanisms on the rotor blade as well as in the stationary rotor frame (Refs. 1, 2). Active rotors in some form are constantly under investigation, some of the most recent examples include the META rotor system-based individual blade control (Ref. 3) and the STAR rotor system for active twist control (Ref. 4).

Rotorcraft manufacturers tend to strive towards reducing the number of parts that make up the rotor system in order to reduce maintenance costs. Adding active control capability tends to increase the number of parts. The *raison d'être* of installing both on-blade and off-blade active

rotor control mechanisms is to improve rotor efficiency such that any potential increase in maintenance costs is justified. Additionally, a few studies have even focussed on using on-blade active control mechanisms for primary rotor control thereby doing away with the conventional swashplate mechanism (Refs. 5–7).

These ongoing efforts emphasise the need for updated and improved modelling techniques for such systems. To that end, rotor comprehensive analysis using Dymore (Ref. 8) coupled with a viscous vortex particle method (VVPM) formulation is proposed. An example on-blade active camber morphing mechanism (Ref. 9) is investigated in this study but the proposed setup can be used, for e.g., for individual blade control studies without any modifications. For this purpose the VVPM formulation is verified using results presented in literature. Coupled Dymore+VVPM results are presented for a simple wing case in order to assess the ability of VVPM to accurately model the unsteady effects of the wing wake, both due to pitching of the wing as well as active morphing, on the wing itself.

Paper submitted to the 39th European Rotorcraft Forum, Bueckeburg, Germany, September 5–7, 2023.

METHODOLOGY

Dymore

Dymore is a comprehensive analysis code that allows representation of the rotor topology with high fidelity. This is accomplished via a library of multibody components such as beams, cables, shells etc and different joints and constraint modelling abilities. Physical and geometric properties can be defined for all joints as well as bodies connecting the joints. Figure 1 illustrates the topology of the Bo 105 main rotor system used in the current study together with relevant reference frames. Note that the figure is not to scale in order to show the rotor drive train in sufficient detail. Details corresponding to the reference frames and the geometry of the various drive-train components are provided in Tables 1 and 2. An elastic fuselage is not modeled. Therefore, the end of the shaft is rigidly fixed with respect to an inertial frame.

The rotor blade structure is modeled as a one-dimensional beam using a geometrically exact formulation. The finite-element discretisation of the rotor blade consists of 14 elements and linear shape function distributed equally throughout the blade.

The rotor aerodynamics solution is obtained by separate blade and wake aerodynamic models - inner and outer problem approach (Ref. 10). The blade aerodynamics solution requires steady airfoil C_l , C_d and C_m data in the form of C81 tables for a range of angles of attack and Mach number that are expected to occur on the blade sections of the rotor. For the current study, the tables were already generated in a previous study were used and the details can be found here in Refs. 11, 12. The quasi steady blade aerodynamic loads were obtained by solving for the complete rotor multibody structural dynamics and obtaining the system configuration at each time step. The instantaneous blade angle of attack and Mach number was obtained using the local flow velocity relative to the quarter-chord of each blade section. With Lagrangian polynomial interpolation (Ref. 13) between the discrete C81 table entries, the instantaneous aerodynamic lift, drag and moment at each blade section is evaluated. Correction of lift, drag (due to unsteady lift) and moment due to unsteady effects, if needed, was carried out using the Peters finite-state unsteady aerodynamic model for flexible airfoils (Ref. 14). No correction was applied to account for the effect of blade spanwise flow on 2D section steady as well as unsteady aerodynamics except that the interpolated section drag coefficient was obtained based on flow Mach number that includes the spanwise radial flow.

The rotor wake effects were separately incorporated using the wake induced velocity on the blade sections using the Peters-He inflow model. The model is based on detailed analytical derivations and simplifications that can make concise descriptions in Refs. (Refs. 15, 16), the first publications that discuss the model, difficult to

follow. Refs. 17 and 18 cover some of the details skipped in the original publications of the model and clarify some of the typos. The inflow velocity evaluated at the blade sections during previous time step was used to evaluate the angle of attack at the current time step. This inflow model has been validated using experimental data in a number of flight scenarios and different rotors.

Once the rotor aerodynamics is solved for at each time step, the aerodynamic forces and moments on each blade section are transformed to the blade structural nodes in order to fill the external forcing matrix of the multibody model. The simulation progresses by repeating the above process of obtaining the airloads for the next time step. In order to achieve a trimmed rotor simulation, an autopilot controller (Ref. 19) based on Ref. 20 was used.

In order to model active wing aerodynamics, Dymore includes possibility to include 'compound' airfoil tables. Here, in order to obtain instantaneous quasi-steady airfoil aerodynamic coefficients the interpolation scheme involves an additional variable such as the trailing-edge flap deflection. The 2D unsteady aerodynamic model of Ref. 14 already includes the possibility to model unsteady aerodynamic effects of airfoil morphing. However, this model requires a separate wake model in order to evaluate the wake-induced inflow on the blade sections. In the case of rotor analysis this requirement is fulfilled using the Peters-He inflow model. In the case of a wing analysis, the Peters 2D dynamic inflow model introduced in (Ref. 21) is used in order to obtain the inflow due to the flat wake behind the wing.

Viscous vortex particle method

The viscous vortex particle method (VVPM) solves the incompressible Navier-Stokes equations. For this it uses the vorticity formulation of the equations where the pressure variable has been eliminated:

$$\frac{\partial \omega}{\partial t} + (\mathbf{u} \cdot \nabla) \omega - \omega \cdot \nabla \mathbf{u} = \nu \Delta \omega \quad (1)$$

The formulation naturally lends itself to generation and convection of particles in the Lagrangian frame. The domain of investigation of fluid flow around a body of interest is also limited to the region where vorticity in the flow, represented using particles, dominates. As a consequence, this methodology gained traction as an alternative to grid-based computational fluid dynamic techniques. Ref. 22(Chapter 1) provides a concise modern review of the origins and the development of vortex methods with particular focus on vortex particle methods. In the current study, the unsteady wake is modelled using the viscous vortex particle method as detailed in Refs. 23 and 24. The most relevant elements of the formulation are detailed in this section for the sake of completeness and accuracy. Refs. 22(Section 2.5), and

25(Appendix A) describe the mathematical basis of discretising a function, the vorticity field distribution in particular, using particles. The fundamental idea revolves around using the Dirac delta distribution and appropriate weights to sample any given function over a domain.

$$\omega(\mathbf{x}, t) \approx \sum_p \alpha_p(t) \delta(\mathbf{x} - \mathbf{x}_p(t)) \quad (2)$$

where

$$\int \omega(\mathbf{x}, t) d\mathcal{V} \approx \sum_p \alpha_p(t) \quad (3)$$

α_p corresponds to the strength of the particles and is given by the vorticity at a given location multiplied by the volume, associated with that particle, based on the discretization scheme. In order to avoid large induced velocities when two particles get close to each other, the standard practice includes 'mollifying' the Dirac delta function-based singular vorticity field using a smooth cutoff function ζ . The mollified or regularised vorticity field ω_σ , as is often referred to in literature, is given by

$$\begin{aligned} \omega(\mathbf{x}, t) &\approx \omega_\sigma(\mathbf{x}, t) = \zeta_\sigma * \omega(\mathbf{x}, t) \\ &= \sum_p \alpha_p(t) \zeta_\sigma(\mathbf{x} - \mathbf{x}_p(t)) \end{aligned} \quad (4)$$

$$\zeta_\sigma(\mathbf{x}) = \frac{1}{\sigma^3} \zeta\left(\frac{|\mathbf{x}|}{\sigma}\right) \quad (5)$$

ζ_σ here is referred to as a regularisation function.

The problem of flow field solution in time using VVPM is a classic N -body problem where N refers to the entity of interest, vortex particles in this case, within the formulation. Given that each particle influences every other particle within the domain, the computational complexity is of $\mathcal{O}(N^2)$. While there are both algorithmic acceleration techniques as well as hardware architecture solutions available for achieving execution speed-up, the current formulation only uses multiple CPU cores for OpenMP-based parallelisation (Ref. 26). According to Ref. 25(Section 2.2), the efficiency of the vortex methods is contingent on the choice of regularisation function ζ_σ and the initialisation of particle strength and position. For the purposes of the current investigation, the regularisation functions were based on those suggested in Ref. 24. The Gaussian kernel was used for Dymore+VVPM coupled analysis while the higher-order algebraic kernel was used for verifying the VVPM model.

The evolution of the vortex particles occurs with interparticle interactions that lead to change in particle strengths, α_{p_i} , as well as velocity induced in accordance with the Biot-Savart law. Accordingly, the evolution equations can be written as follows.

$$\frac{d\mathbf{x}_{p_{ij}}}{dt} = v_\sigma(\mathbf{x}_{p_i}) \quad (6)$$

$$\frac{d\alpha_{p_i}}{dt} = \left(\frac{d\alpha_{p_i}}{dt}\right)_{\text{viscous diffusion}} + \left(\frac{d\alpha_{p_i}}{dt}\right)_{\text{vortex stretching}} \quad (7)$$

where, the induced velocity on a given particle ($v_\sigma(\mathbf{x}_{p_i})$) due to the regularised vorticity field and the rates of change in vortex particle strengths are given as follows.

$$v_\sigma(\mathbf{x}_{p_i}) = \sum_{\substack{j=1 \\ i \neq j}}^{N_p} K_\sigma(\mathbf{x}_{p_{ij}}) \times \alpha_{p_j} \quad (8)$$

$$\begin{aligned} \left(\frac{d\alpha_{p_i}}{dt}\right)_{\text{viscous diffusion}} &= \nu \nabla^2 (\mathcal{V} \omega_{\sigma_i}) \\ &= \frac{2\nu}{\sigma^2} \sum_{j=1}^{N_p} (\mathcal{V}_{p_i} \alpha_{p_j} - \mathcal{V}_{p_j} \alpha_{p_i}) \eta_\sigma(|\mathbf{x}_{p_{ij}}|) \end{aligned} \quad (9)$$

$$\begin{aligned} \left(\frac{d\alpha_{p_i}}{dt}\right)_{\text{vortex stretching}} &= \sum_{j=1}^{N_p} \left[\frac{q_\sigma(|\mathbf{x}_{p_{ij}}|)}{x_{p_{ij}}^3} (\alpha_{p_i} \times \alpha_{p_j}) \right. \\ &\quad \left. + \{x_{p_{ij}} \cdot (\alpha_{p_i} \times \alpha_{p_j})\} x_{p_{ij}} F_\sigma(|\mathbf{x}_{p_{ij}}|) \right] \end{aligned} \quad (10)$$

The different kernel functions involved in the above expressions are related to the cutoff function ζ by the following results.

$$-\frac{1}{\rho} \frac{d}{d\rho} \zeta(\rho) = \eta(\rho) \quad (11)$$

$$\eta_\sigma(|\mathbf{x}|) = \eta(|\mathbf{x}|/\sigma)/\sigma^3 \quad (12)$$

$$\frac{1}{\rho^2} \frac{d}{d\rho} q(\rho) = \zeta(\rho) \quad (13)$$

$$q_\sigma(|\mathbf{x}|) = q(\rho) \quad (14)$$

$$\rho = \frac{|\mathbf{x}|}{\sigma} \quad (15)$$

$$F_\sigma(|\mathbf{x}|) = \frac{1}{|\mathbf{x}|} \frac{\partial}{\partial s} \left(\frac{q_\sigma(|\mathbf{x}|)}{|\mathbf{x}|^3} \right) = \frac{1}{s^2} \left[\zeta_\sigma(|\mathbf{x}|) - 3 \frac{q_\sigma(|\mathbf{x}|)}{|\mathbf{x}|^3} \right] \quad (16)$$

Based on the type of function used to represent the smooth cutoff function for the particle-based discretization of the vorticity field, the aforementioned kernels can take different forms as shown in Table 3. Here, the regularisation functions are based on those proposed in Ref. 24 for their convergence properties. The HOA-based kernels are used for verification of the methodology using diagnostics while the Gaussian-based kernels are used for the coupled Dymore+VVPM analysis.

Coupling

Dymore has been coupled to VVPM such that the blade aerodynamics is evaluated using airfoil tables-based approach within Dymore and the resulting blade bound circulation is used as an input to the VVPM solver. The generation and development of the wake is then dictated by the Helmholtz laws and Eqs. 6 and 7.

The blade aerodynamics model in Dymore is based on lifting-line theory. Each blade section cross-section has an 'airstation' defined at its quarter-chord location. Based on the wing kinematics and flow field conditions, the section angle of attack is obtained using flow conditions at these airstations. Since the airstations can be arbitrarily defined in the Dymore setup, an interpolation scheme was adopted so that particles were not released behind each airstation but rather uniformly across the lifting-line in accordance with constraint of uniform overlap of particles (Ref. 27). Additionally, in order to separate the spatial and temporal dependence of the vortex particles a new scheme was implemented to ensure that the particle overlap remains constant irrespective of spatial resolution of the particles or the time step size. Figure 2 shows that this discretization was achieved not by placing particles knowing the current and the past trailing-edge positions $TE_k(t_n)$ and $TE_k(t_n + 1)$, respectively, but rather the interpolated trailing-edge positions $TE_k(t_n)$ at the current time step and the position of the last particle that was generated from that point. New particles are then linearly added until the distance between $TE_k(t_n)$ and the latest particle becomes less than h_{res} - where h_{res} is the resolution parameter used to denote the distance between two neighboring particles at the time of their birth. Following the approach in Ref. 23, vortex particles representing trailing vorticity were generated at the trailing-edge between the wing tips at a separation of $2h_{res}$ and particle representing shed vortices were placed in between them - thereby bringing the overall wake resolution to h_{res} . In case only trailing vorticity or only shed vorticity needs to be modelled, then accordingly the number of corresponding particles can be increased such that the wake resolution of h_{res} is maintained.

The coupling between Dymore and the VVPM solver is established such that exchange of information occurs at each time step. Any number of lifting-lines and corresponding airstations can be defined within the Dymore standalone model. For the purposes of coupling with VVPM, the airstation positions need to be augmented with trailing-edge position at the corresponding blade section. This is needed in order to solve for the instantaneous blade/wing trailing-edge positions accounting for an elastic deformation and blade/wing motion. Corresponding to each airstation, the following quantities are passed to VVPM so that interpolated results can be obtained at any given spanwise location - bound circulation, trailing-edge position, far field oncoming flow ve-

locity, and the wing/blade span discretization in order to carry out interpolation. All the passed information is evaluated in the inertial frame of reference. In turn, the wake solver returns the induced flow velocity, due to all the particles in the wake, evaluated at each airstation location, in the inertial frame of reference.

RESULTS AND DISCUSSION

Experimental measurements of the full-scale Bo105 rotor (Ref. 28) were used for validating the baseline Dymore rotor model. It is worth noting that the test campaign, whose results are presented in the aforementioned report, was carried out in 1994 but the results were only made public in 2020. To best of the first author's knowledge, this is the first time full-scale Bo105 rotor simulations have been conducted at the test conditions mentioned in this report and then compared with these published measurements.

The VVPM setup was verified by comparing simulation diagnostics, as mentioned earlier, corresponding results presented in literature (Refs. 27, 29). The VVPM+Dymore framework was validated using the case of an elliptical wing at a static angle of attack and a pitching/morphing rectangular wing.

Dymore model validation

The detailed multibody model setup in Dymore (Fig. 1) was initially verified using the fanplot diagram (Fig. 3) and the results were compared to data available in Ref. (Ref. 30) and that shared by DLR.

The test campaign for which results are reported in Ref. 28 was primarily focussed on individual blade control (IBC). However a number of baseline rotor test runs were made before IBC tests and it is those measurement data that are used for the purposes of validation of the baseline rotor. In fact, all the baseline rotor measurement cases with a forward shaft tilt in Ref. 28 have been used for simulations within Dymore and the results are shown in Figs. 5-8. The trends between the measurement and prediction match reasonably well. However, the match between measurement and Dymore results in the time-domain, over one rotor revolution, is generally poor. This is likely due to the nature of the Peters-He inflow model that Dymore uses in order to model the rotor inflow. The Peters-He model is based on potential flow theory and is an unlikely modelling strategy that will result in simulation results of good fidelity, especially when the focus is to accurately capture the evolution of blade structural loads over the rotor azimuth.

It is envisaged that this can be accomplished using a higher fidelity wake model like the VVPM that directly models the vorticity in the wake and can potentially model even blade-vortex interaction scenarios, something that the Peters-He model is not capable of.

VVPM verification

Model vortex rings based on Eq 17 and data in Table 4 were used to verify the VVPM setup by comparing the predicted diagnostic quantities with those obtained from Refs. 27 and 29.

$$\omega(\mathbf{x}, 0) = \omega(r, \theta, 0) \hat{\mathbf{e}}_\phi = \frac{\Gamma}{2\pi\sigma_R^2} \left(1 + \frac{r}{R} \cos \theta\right) e^{-r^2/2\sigma_R^2} \hat{\mathbf{e}}_\phi \quad (17)$$

Figure 9 details the discretization strategy adopted in order to model the analytical vortex ring of Eq. 17 using VVPM. The number of particles in each layer is $8n$ where n is the order of the layer. Each ring is represented using the number of cross-section layers and the number of azimuthal layers; for e.g., the ring with $n_c = 4$ and $\Delta\phi = 4.5^\circ$ is addressed as '4by80'. For e.g. Fig. 10 shows the 4by80 discretized vortex ring of Eq. 17.

A number of diagnostic quantities from Ref. 27 were used to verify the VVPM model setup: \mathbf{I} - linear impulse; Ω - total vorticity; \mathbf{A} - angular impulse; \mathcal{H}_σ - semi-regularised helicity; E_σ and $E_{\sigma f}$ - semi-regularised and divergence-free kinetic energy, respectively; \mathcal{E}_σ and $\mathcal{E}_{\sigma f}$ - semi-regularised and divergence-free enstrophy, respectively.

$$\mathbf{I} = \frac{1}{2} \sum_{i=1}^{N_p} (\mathbf{x}_{p_i} \times \alpha_{p_i}) \quad (18)$$

$$\Omega = \sum_{i=1}^{N_p} \alpha_{p_i} \quad (19)$$

$$\mathbf{A} = \frac{1}{3} \sum_{i=1}^{N_p} \mathbf{x}_{p_i} \times (\mathbf{x}_{p_i} \times \alpha_{p_i}) \quad (20)$$

$$\mathcal{H}_\sigma = \int (\boldsymbol{\omega} \cdot \mathbf{v}_\sigma) d\mathcal{V} = \sum_{i,j=1}^{N_p} \frac{q_\sigma(\mathbf{x}_{p_{ij}})}{|\mathbf{x}_{p_{ij}}|} [\mathbf{x}_{p_{ij}} \cdot (\alpha_{p_i} \times \alpha_{p_j})] \quad (21)$$

$$E_\sigma = \frac{1}{2} \int (\mathbf{v} \cdot \mathbf{v}_\sigma) d\mathcal{V} = \frac{1}{16\pi} \sum_{i,j=1}^{N_p} \frac{(|\mathbf{x}_{p_{ij}}|^2 + 2\sigma^2) \alpha_{p_i} \cdot \alpha_{p_j} + (\mathbf{x}_{p_{ij}} \cdot \alpha_{p_i}) (\mathbf{x}_{p_{ij}} \cdot \alpha_{p_j})}{(\sigma^2 + |\mathbf{x}_{p_{ij}}|^2)^{3/2}} \quad (22)$$

$$E_{\sigma f} = \frac{1}{2} \int \boldsymbol{\psi}_\sigma \cdot \boldsymbol{\omega} dx = \frac{1}{2} \sum_{i,j=1}^{N_p} G_\sigma(\mathbf{x}_{p_i} - \mathbf{x}_{p_j}) \alpha_{p_i} \cdot \alpha_{p_j} = \frac{1}{8\pi} \sum_{i,j=1}^{N_p} \frac{(|\mathbf{x}_{p_i} - \mathbf{x}_{p_j}|^2 + \frac{3}{2}\sigma^2)}{(|\mathbf{x}_{p_i} - \mathbf{x}_{p_j}|^2 + \sigma^2)^{\frac{3}{2}}} \alpha_{p_i} \cdot \alpha_{p_j}. \quad (23)$$

$$\mathcal{E}_\sigma = \int (\boldsymbol{\omega} \cdot \boldsymbol{\omega}_\sigma) d\mathcal{V} = \frac{1}{8\pi} \sum_{i,j=1}^{N_p} \frac{1}{(|\mathbf{x}_{p_{ij}}|^2 + \sigma^2)^{9/2}} [(|\mathbf{x}_{p_{ij}}|^2 + \sigma^2)(2|\mathbf{x}_{p_{ij}}|^4 + 7\sigma^2|\mathbf{x}_{p_{ij}}|^2 + 20\sigma^4)(\alpha_{p_i} \cdot \alpha_{p_j}) - 3(2|\mathbf{x}_{p_{ij}}|^4 + 9\sigma^2|\mathbf{x}_{p_{ij}}|^2 + 7\sigma^4)(\mathbf{x}_{p_{ij}} \cdot \alpha_{p_i})(\mathbf{x}_{p_{ij}} \cdot \alpha_{p_j})] \quad (24)$$

$$\mathcal{E}_{\sigma f} = \int \boldsymbol{\omega} \cdot \boldsymbol{\omega}_\sigma d\mathbf{x} = \sum_{i,j=1}^{N_p} \zeta_\sigma(\mathbf{x}_{p_i} - \mathbf{x}_{p_j}) \alpha_{p_i} \cdot \alpha_{p_j} = \frac{1}{4\pi} \sum_{i,j=1}^{N_p} \frac{15}{2} \frac{\sigma^4}{(|\mathbf{x}_{p_i} - \mathbf{x}_{p_j}|^2 + \sigma^2)^{\frac{7}{2}}} \alpha_{p_i} \cdot \alpha_{p_j} \quad (25)$$

Table 5 presents various diagnostic results at time $t = 0$ s for three different discretization cases of 4by80, 5by100 and 6by117, respectively. Different iterative schemes adopted, in order to obtain the initial strengths of the vortex particles, could be the source of the differences in the initial diagnostics across the different studies. As the vortex ring discretization resolution is increased the diagnostic results approach the analytical results available for vortex ring of Eq. 17 and are given in Ref. 23. Figures 11, 12 and 13 show the time-domain development of the simulation by showing diagnostics for which corresponding data is available in literature. Ref. 27 showed additional results corresponding to fusion of two 3by49 rings and fusion-fission of two 2by52 rings in order to assess the ability of the vortex method to model viscous processes. The visualisation of these two cases and the evolution of their respective diagnostics are shown in Figs. 14-17.

Dymore+VVPM coupling

The coupling between the structural dynamics and blade aerodynamics solver Dymore and the wake solver VVPM was established as detailed earlier. The coupled framework was verified using static analysis as well as dynamic analysis.

For the static case, an elliptical rigid pitching wing was modelled in Dymore using the geometry provided in Ref. 29. Based on lifting-line analysis, the velocity induced by the trailing vortices on an elliptical wing is constant over the entire span (see Ref. 31, Section 5.5.3) and is related to the wing geometry and the lift generated by the wing as follows-

$$L = \frac{\rho V \Gamma_{b,mid} \pi s}{4} \quad (26)$$

$$L = C_L \frac{1}{2} \rho V^2 S \quad (27)$$

$$\Gamma_{b,mid} = \frac{2C_L V S}{\pi s} \quad (28)$$

$$v_{ind} = \frac{\Gamma_{b,mid}}{2s} \quad (29)$$

Here, S is the total wing area and s is the wing span.

For the elliptic wing validation case the effect of the inflow on the wing section angle of attack was ignored while evaluating the section bound circulation within Dymore. Only a one way coupling was used in order to be consistent with the analytical results used for comparison. Figure 18 shows the wing geometry and the resultant wake. The induced velocity generated over the wing span is shown in Fig. 19 and compared with the theoretical result considering wing section $C_l = 0.527$ at $\alpha = 5^\circ$.

In order to validate the ability of VVPM to model the influence of the unsteady wake on the wing as well as to investigate the potential of the current framework for use in active rotor studies, two separate dynamic cases were modelled - a pitching wing and a wing with active camber morphing. The geometry of the rectangular wing used for this purpose is shown in Fig. 20(a) with the camber morphing mechanism in action. The span and chord here was kept the same as the elliptical wing case. The wake modelled using the particle method is shown in Fig. 20(b). No trailing particles were modelled for this analysis so that comparison with corresponding results from Dymore, which modelled only 2D unsteady effects, could be made.

$$\alpha = 5^\circ \sin(5 * 2 * \pi t) \quad (30)$$

$$\delta = 9^\circ \sin(10 * 2 * \pi t) \quad (31)$$

Figure 21 shows the wake-induced velocity variation at the wing mid-section over one time period (based on a 5Hz cycle) based on both Dymore and Dymore+VVPM framework. In case of the Dymore standalone model, the Peters 2D unsteady aerodynamic model (Ref. 14) and 2D dynamic inflow model (Ref. 21) were used for this purpose. Note that Dymore version 4.1, that was used in the current study, lacks the ability to model 2D dynamic inflow for active wings and so the capability was accordingly incorporated. A characteristic that stands out from Fig. 21 is the jittery nature of the induced velocity at the wing mid-section over time. This can be attributed to the discretization scheme adopted for introduction of particles whereby the location of the youngest particles p_k (see Fig. 2) can shift slightly in the chordwise direction from one time step to the next. Since these nearest particles, nearest to the wing, have the highest influence on the induced velocity on the wing, any small deviation can manifest as a visible effect on

the wing induced velocity. This jitter can be minimised by increasing the particle resolution i.e. decreasing h_{res} .

The close match between the wake induced inflow predicted using Dymore+VVPM and using potential flow theory-based models should not be taken as an indicator of the futility of particle-based methods. The current investigation will be expanded in the future to model full-scale active rotors in different flight conditions and it is envisaged that the verified and validated Dymore+VVPM framework established here would be uniquely suited to model unsteady effects of the 3D wake generated in that scenario - something that cannot be accurately captured only using 2D unsteady wake models.

CONCLUSION

A multibody model of the full-scale Bo105 rotor was created using the aeromechanics analysis solver Dymore. This model was verified by comparing predicted hubloads and bladeloads with experimental measurements. A coupled analysis framework has been established with Dymore and a viscous vortex particle formulation. This setup was validated using an elliptical static wing setup and comparing the predicted induced velocities on the wing quarter-chord against analytical results. In order to assess the potential of the Dymore+VVPM setup for predicting unsteady wake effects, a rectangular wing with pitching as well as a static rectangular wing with dynamic camber morphing were used. The induced velocities in either case were compared to inflow velocity obtained using the finite-state 2D inflow model.

Overall, the validated results from the Dymore standalone model and the ability of the Dymore+VVPM setup to better predict 3D/2D wake effects instill confidence that the coupled framework can be reliably used for active rotor studies. Work on this front is currently ongoing.

ACKNOWLEDGEMENTS

This work was sponsored by the European Union's Horizon 2020 research and innovation program under grant agreement number 723491 and by the LuFo VI-2 program of the German Federal Ministry for Economic Affairs and Climate Action under grant number 20E2108A. The first author would also like to thank Puneet Singh for sharing parts of his own particle wake code and for taking the time to share his expertise on the subject.

Supported by:



on the basis of a decision
by the German Bundestag

REFERENCES

1. Mueller, M., Arnold, U., and Morbitzer, D., "On the Importance and Efficiency of 2/rev IBC for Noise, Vibration and Pitch Link Load Reduction," 25th European Rotorcraft Forum, Rome, Italy, September 1999.
2. Jacklin, S. A., Blaas, A., Teves, D., Kube, R., and Warmbrodt, W., "Reduction of Helicopter BVI noise, Vibration, and Power consumption through Individual Blade Control," AHS 51st Annual Forum and Technology Display, Fort Worth, TX, May 1994.
3. Küfmann, P., Bartels, R., van der Wall, B. G., Schneider, O., Holthusen, H., and Postma, J., "Individual blade control of a 5-bladed rotor using the multiple swashplate system," 43rd European Rotorcraft Forum, Milano, Italy, September 2017.
4. van Der Wall, B. G., Lim, J. W., Riemenschneider, J., Kalow, S., Wilke, G. A., Boyd, D. D., Bailly, J., Delrieux, Y., Cafarelli, I., Tanabe, Y., Sugawara, H., Jung, S. N., Hong, S. H., Kim, D.-H., Kang, H. J., Barakos, G., and Steininger, R., "Smart Twisting Active Rotor (STAR)-Pre-Test Predictions," 48th European Rotorcraft Forum, Winterthur, Switzerland, September 2022.
5. Falls, J., Datta, A., and Chopra, I., "Integrated Trailing-Edge Flaps and Servotabs for Helicopter Primary Control," *Journal of the American Helicopter Society*, Vol. 55, (3), 2010.
6. Thornburgh, R. P., Kreshock, A. R., Wilbur, M. L., Sekula, M. K., and Shen, J., "Continuous trailing-edge flaps for primary flight control of a helicopter main rotor," American Helicopter Society 70th Annual Forum, Montréal, Canada, May 2014.
7. Chaudhry, Z., Wake, B., Bagai, A., Lorber, P., and Collons, A., "Active rotor development for primary and secondary flight control," American Helicopter Society 65th Annual Forum & Technology Display, Grapevine, TX, May 2009.
8. Bauchau, O. A., "DYMORE user's manual," *Georgia Institute of Technology, Atlanta*, 2007.
9. Woods, B. K., Dayyani, I., and Friswell, M. I., "Fluid/structure-interaction analysis of the fishbone-active-camber morphing concept," *Journal of Aircraft*, Vol. 52, (1), 2015, pp. 307–319.
10. Johnson, W., *Rotorcraft Aeromechanics*, Cambridge University Press, New York, NY, 2013.
11. Abdelmoula, A., and Rauleder, J., "Aerodynamic performance of morphed camber rotor airfoils," AIAA Scitech 2019 Forum, San Diego, CA, January 2019. DOI: 10.2514/6.2019-1101
12. Komp, D., Kumar, S., Hajek, M., and Rauleder, J., "Effect of Active Camber Morphing on Rotor Performance and Control Loads," *Aerospace Science and Technology*, 2020. DOI: 10.1016/j.ast.2020.106311
13. Burden, R. L., and Faires, J. D., *Numerical analysis*, Brooks/Cole Cengage learning, Boston, Massachusetts, 2011.
14. Peters, D. A., Hsieh, M.-c. A., and Torrero, A., "A State-Space Airloads Theory for Flexible Airfoils," *Journal of the American Helicopter Society*, Vol. 52, (4), 2007, pp. 329–342.
15. Peters, D. A., and He, C. J., "Finite state induced flow models. II-Three-dimensional rotor disk," *Journal of Aircraft*, Vol. 32, (2), 1995, pp. 323–333. DOI: 10.2514/3.46719
16. He, C., *Development and Application of a Generalized Dynamic Wake Theory for Lifting Rotors*, Ph.D. thesis, Georgia Institute of Technology, July 1989.
17. Murakami, Y., *A new appreciation of inflow modelling for autorotative rotors*, Ph.D. thesis, University of Glasgow, October 2008.
18. Banerjee, T., *Dynamic Inflow-based Analysis of Pitch Changes to Hovering Rotor*, Master's thesis, Nanyang Technological University, September 2020.
19. Bauchau, O., "Dymore Manual," <https://www.dymoresolutions.com/ControllerElements/AutoPlt.html/>, [Online; accessed 21-August-2023], 2023.
20. Peters, D. A., Barwey, D., *et al.*, "A general theory of rotorcraft trim," *Mathematical Problems in Engineering*, Vol. 2, 1996, pp. 1–34.
21. Peters, D. A., Karunamoorthy, S., and Cao, W.-M., "Finite state induced flow models. I-Two-dimensional thin airfoil," *Journal of aircraft*, Vol. 32, (2), 1995, pp. 313–322. DOI: 10.2514/3.46718
22. Kirchhart, M., *Vortex Particle Redistribution and Regularisation*, Ph.D. thesis, Keio University, August 2017.
23. Singh, P., *Aeromechanics of Coaxial Rotor Helicopters using the Viscous Vortex Particle Method*, Ph.D. thesis, University of Michigan, October 2020.
24. Winckelmans, G., and Leonard, A., "Contributions to vortex particle methods for the computation of three-dimensional incompressible unsteady flows," *Journal of Computational Physics*, Vol. 109, (2), 1993, pp. 247–273.

25. Cottet, G.-H., and Koumoutsakos, P. D., *Vortex Methods: Theory and Practice*, Cambridge university press, 2000.
26. "OpenMP," <https://www.openmp.org/>, [Online; accessed 21-August-2023], 2023.
27. Winckelmans, G. S., *Topics in vortex methods for the computation of three- and two-dimensional incompressible unsteady flows*, Ph.D. thesis, California Institute of Technology, February 1989.
28. Jacklin, S. A., Swanson, S., Blaas, A., Richter, P., Teves, D., Niesl, G., Kube, R., Gmelin, B., and Key, D. L., "Investigation of a Helicopter Individual Blade Control (IBC) System in Two Full-Scale Wind Tunnel Tests: Volume II—Tabulated Data," Technical Report TP-20205003457 Vol II, NASA, July 2020.
29. Valentin, J., Moretti, R., and Bernardos, L., "Development of an Aerodynamic Simulation Technique Based on the Vortex Particle Method," PEGASUS Conference, Pise, Italy, April 2022.
30. Warmbrodt, W., and Peterson, R. L., "Hover Performance and Dynamics of a Full-Scale Hingeless Rotor," Technical Report TM 85990, NASA, August 1984.
31. Houghton, E. L., Carpenter, P. W., Collicott, S. H., and Valentine, D. T., *Aerodynamics for Engineering Students*, Elsevier, 2013.
32. Goulos, I., *Simulation Framework Development for the Multidisciplinary Optimisation of Rotorcraft*, Ph.D. thesis, 2012.

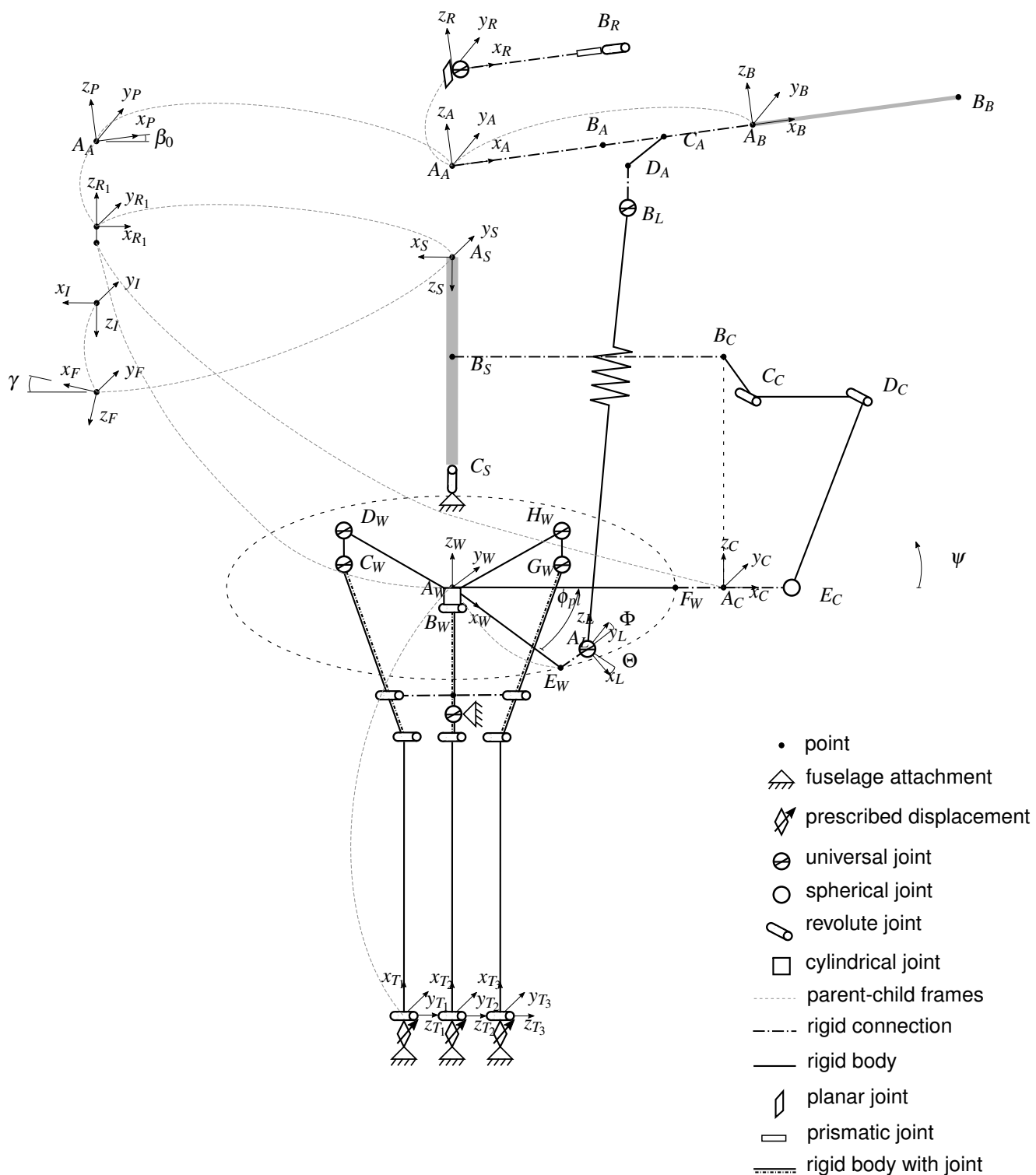


Figure 1: Illustration of the multibody dynamics model of the Bo 105 rotor in Dymore. Note that the illustration is not to scale.

Table 1: Details of the Bo 105 multibody model of Fig. 1. Fixed points represented as • and joints as .

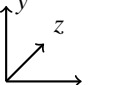
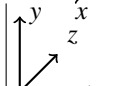
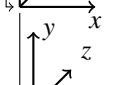
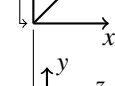
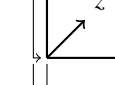
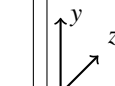
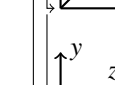
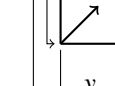
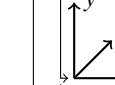

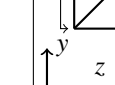
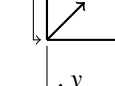
Frame name	Definition	Relevant points
Inertial I		
Fuselage F	 $I\bar{e}_{F,y}^T = \{0, 1, 0\}$ $I\bar{e}_{F,z}^T = \{\sin(\gamma), 1, \cos(\gamma)\}$ $I O_F = \{0, 0, 0\}$	
Shaft S	 $F\bar{e}_{S,y}^T = \{0, 1, 0\}$ $F\bar{e}_{S,z}^T = \{-\sin(\gamma), 1, \cos(\gamma)\}$ $F O_S = \{0, 0, 0\}$	<ul style="list-style-type: none"> • $sA_S = \{0, 0, 0\}$ • $sB_S = \{0, 0, z_{sc}\}$ • $sC_S = \{0, 0, l_{sh}\}$
Root R_i	 $s\bar{e}_{R_i,y}^T = \{\sin(\Delta\theta_i), \cos(\Delta\theta_i), 0\}$ $s\bar{e}_{R_i,z}^T = \{0, 0, -1\}$ $s O_{R_i} = \{0, 0, 0\}$	
Scissor C	 $R_i\bar{e}_{C,y}^T = \{0, 1, 0\}$ $R_i\bar{e}_{C,z}^T = \{0, 0, 1\}$ $R_i O_C = \{0, 0, -z_{sw}\}$	<ul style="list-style-type: none"> • $cA_C = \{0, 0, 0\}$ • $cB_C = \{0, 0, z_{sw} - z_{sc}\}$ • $cC_C = \{0.03, 0, 0.15\}$ <ul style="list-style-type: none"> • $cD_C = \{0.35, 0, 0.15\}$ • $cE_C = \{r_{sc}, 0, 0\}$
Swashplate W	 $c\bar{e}_{W,y}^T = \{0, 1, 0\}$ $c\bar{e}_{W,z}^T = \{0, 0, 1\}$ $c O_W = \{0, 0, -z_{sw}\}$	<ul style="list-style-type: none"> • $wA_W = \{0, 0, 0\}$ • $wB_W = \{0, 0, z_{sw} - z_{sc}\}$ • $wC_W = \{0.03, 0, 0.15\}$
Servo T_i	 $w\bar{e}_{T_i,y}^T = \{0, 1, 0\}$ $w\bar{e}_{T_i,z}^T = \{0, 0, 1\}$ $w O_{T_i} = \{0, 0, -z_i(2 - i)\}$	
Pitch link L	 $w\bar{e}_{L,y}^T = \{\sin(\Theta) \cdot \sin(\Phi), \cos(\Phi), \cos(\Theta) \cdot \cos(\Phi)\}$ $w\bar{e}_{L,z}^T = \{\sin(\Theta) \cdot \cos(\Phi), -\sin(\Phi), \cos(\Theta) \cdot \cos(\Phi)\}$ $w O_L = \{r_{pl}, 0, 0\}$	<ul style="list-style-type: none"> • $L A_L = \{0, 0, 0\}$ • $L B_L = \{0, 0, l_{pl}\}$
Precone P	 $R_i\bar{e}_{P,y}^T = \{0, 1, 0\}$ $R_i\bar{e}_{P,z}^T = \{-\sin(\beta_0), 0, -\cos(\beta_0)\}$ $R_i O_P = \{0, 0, 0\}$	
Attachment A	 $P\bar{e}_{A,y}^T = \{0, 1, 0\}$ $P\bar{e}_{A,z}^T = \{0, 0, 1\}$ $P O_A = \{0, 0, 0\}$	<ul style="list-style-type: none"> • $pA_A = \{0, 0, 0\}$ • $pB_A = \{e_p, 0, 0\}$ • $pC_A = \{x_{ph}, 0, 0\}$ • $pD_A = \{x_{ph}, y_{ph}, 0\}$
Retention R	 $A\bar{e}_{R,y}^T = \{0, 1, 0\}$ $A\bar{e}_{R,z}^T = \{0, 0, 1\}$ $A O_R = \{0, 0, 0\}$	<ul style="list-style-type: none"> • $RA_R = \{0, 0, 0\}$ • $RB_R = \{0, 0, e_p\}$
Blade B	 $A\bar{e}_{B,y}^T = \{0, 1, 0\}$ $A\bar{e}_{B,z}^T = \{0, 0, 1\}$ $A O_B = \{0, 0, 0\}$	<ul style="list-style-type: none"> • $AB_B = \{0, 0, 0\}$ • $AB_B = \{0.93R, 0, 0\}$

Table 2: Details for Bo 105 rotor system multibody model construction.

	Symbol	Value	Description	
general	N_b	4	number of blades	
	σ	0.0		
	R	4.912 m		
rotor head	γ	3°	shaft tilt angle	
	β_0	2.5°	precone	
	$\Delta\theta_1$	0°	Blade 1	
	$\Delta\theta_2$	90°	Blade 2	
	$\Delta\theta_3$	180°	Blade 3	
	$\Delta\theta_4$	270°	Blade 4	
pitchlink	x_{ph}	0.2 m	radial location of pitchhorn	
	y_{ph}	0.196 m	pitchhorn distance to feathering axis	
	z_{ph}	0	pitchhorn vertical offset	
	e_p	0.221 m	pitch bearing radial position	
	Θ	15°		
	Φ	0°		
	r_{pl}	0.2 m		
	l_{pl}	0.30 m		
	shaft	l_{sh}	0.3 m	
	scissor	z_{sc}	0.1 m	
swashplate	$l_{sc,r}$	0.35 m		
	$l_{sc,v}$	0.15 m		
	$r_{sc,o}$	0.3 m	outer pickup radius	
	$r_{sc,i}$	0.03 m	inner pickup radius	
	z_{sc}	0.35 m		
servos	ϕ_{pl}	45°		
	z_t	0.07 m		

Higher-order algebraic (HOA)	Gaussian
$\zeta(\rho) = \frac{15}{8\pi} \frac{1}{(\rho^2+1)^{7/2}}$	$\zeta(\mathbf{x}) = \frac{1}{(2\pi)^{3/2}} e^{- \mathbf{x} ^2/2}$
$\zeta_\sigma(\mathbf{x}) = \frac{15}{8\pi} \frac{\sigma^4}{(\mathbf{x} ^2+\sigma^2)^{7/2}}$	$\zeta_\sigma(\mathbf{x}) = \frac{1}{(2\pi)^{3/2}\sigma^3} e^{- \mathbf{x} ^2/2\sigma^2}$
$\eta_\sigma(\mathbf{x}) = \frac{105}{8\pi} \frac{\sigma^6}{(\mathbf{x} ^2+\sigma^2)^{9/2}}$	$\eta_\sigma(\mathbf{x}) = \frac{1}{(2\pi)^{3/2}\sigma^3} e^{- \mathbf{x} ^2/2\sigma^2}$
$q_\sigma(\mathbf{x}) = \frac{ \mathbf{x} ^3}{4\pi} \frac{(\mathbf{x} ^2+\frac{5\sigma^2}{2})}{(\mathbf{x} ^2+\sigma^2)^{5/2}}$	$q_\sigma(\mathbf{x}) = \frac{1}{4\pi} \operatorname{erf}\left(\frac{ \mathbf{x} }{\sqrt{2}\sigma}\right) - \frac{ \mathbf{x} }{(2\pi)^{3/2}\sigma} e^{- \mathbf{x} ^2/2\sigma^2}$

Table 3: Different kernel expressions based on the higher-order algebraic and the Gaussian smooth cutoff functions.

Parameter	Isolated vortex ring	Fusion vortex rings	Fusion-fission vortex rings
Vortex ring radius, R_0	1.0	1.0	1.0
Circulation, Γ_v	1.0	1.0	1.0
Core radius, r_c	0.10	0.10	0.10
Discretization core radius, r_0	0.35	0.35	0.35
Time step, Δt	0.025	0.025	0.025
Reynolds number, Re	400	400	200
Kinematic viscosity, ν	2.50×10^{-3}	2.50×10^{-3}	5×10^{-3}

Table 4: Vortex ring parameters

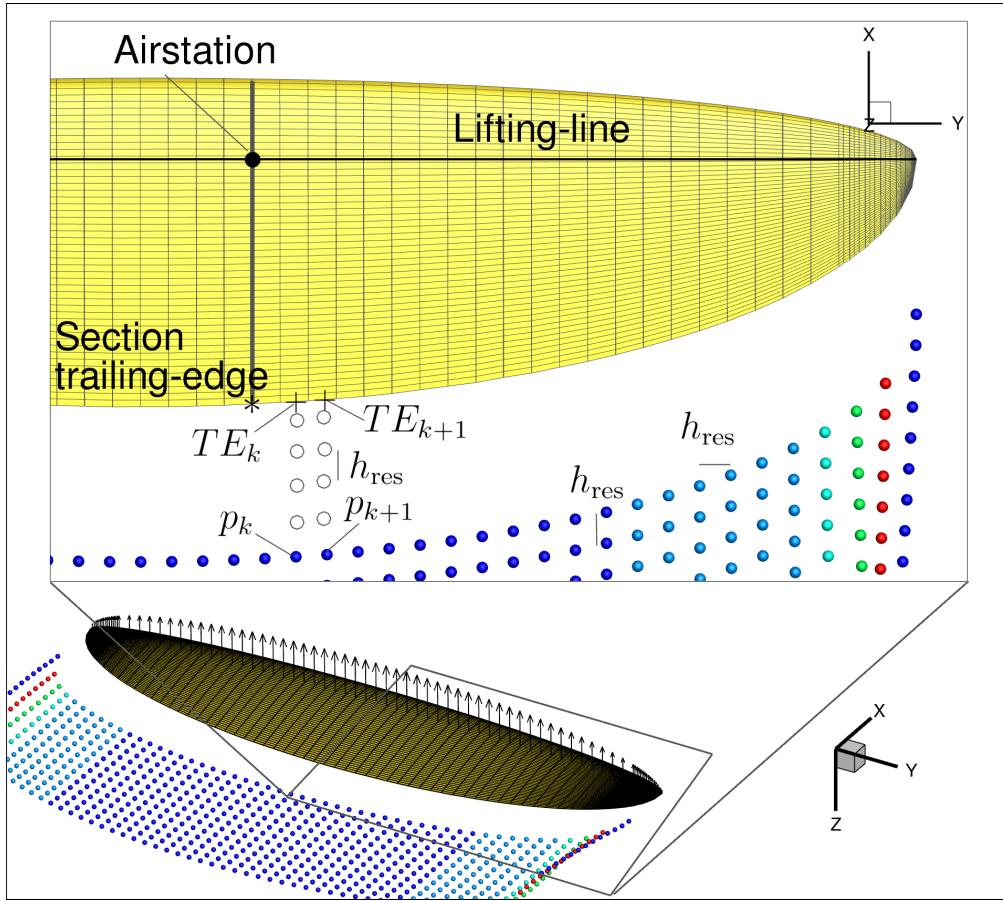


Figure 2: Illustration of the initialisation of position and strength of particles for modelling trailed and shed vorticity.

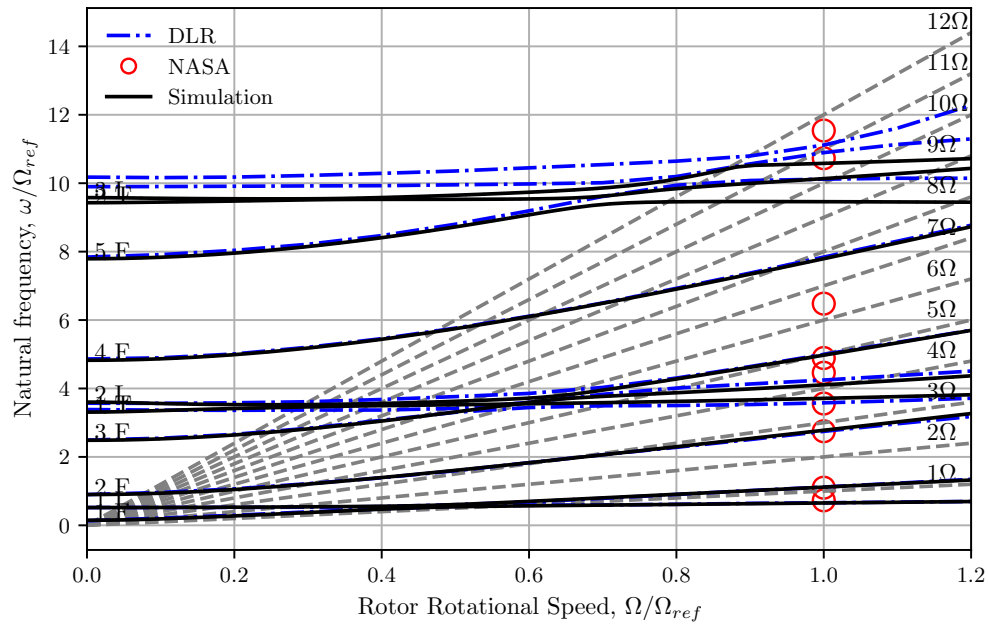


Figure 3: Bo 105 rotor blade frequency fan plot at 0° collective.

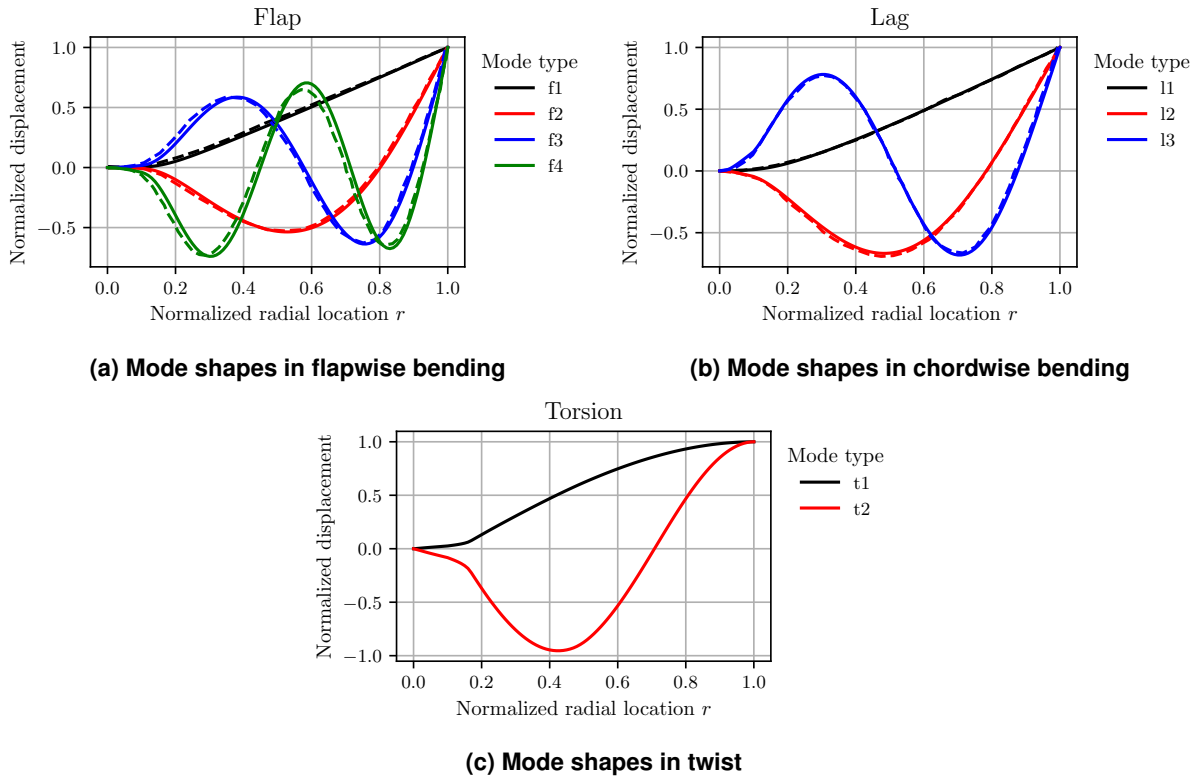


Figure 4: Comparison of the mode shapes obtained using the current simulation (shown using —) versus those provided in Ref. 32 (shown using - - -). Note only flap and lag mode shapes are provided in Ref. 32.

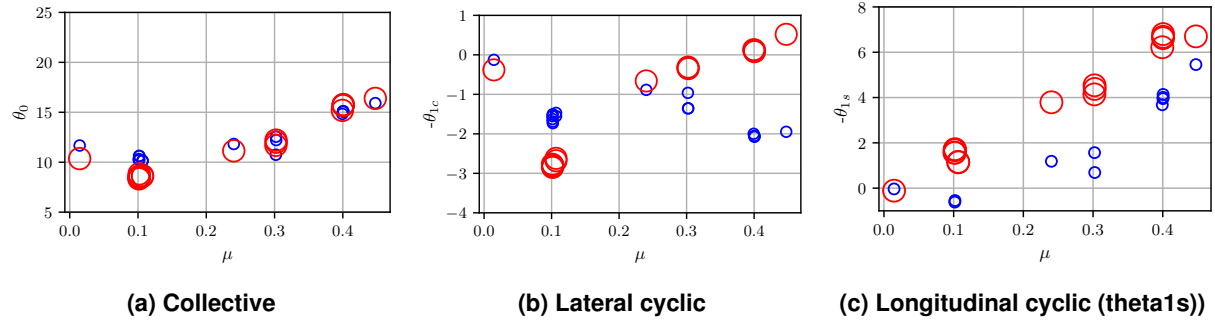


Figure 5: Comparison of Bo 105 rotor control angles between measurements (Ref. 28) and simulation results. \circ - Simulation \circ - Expt.

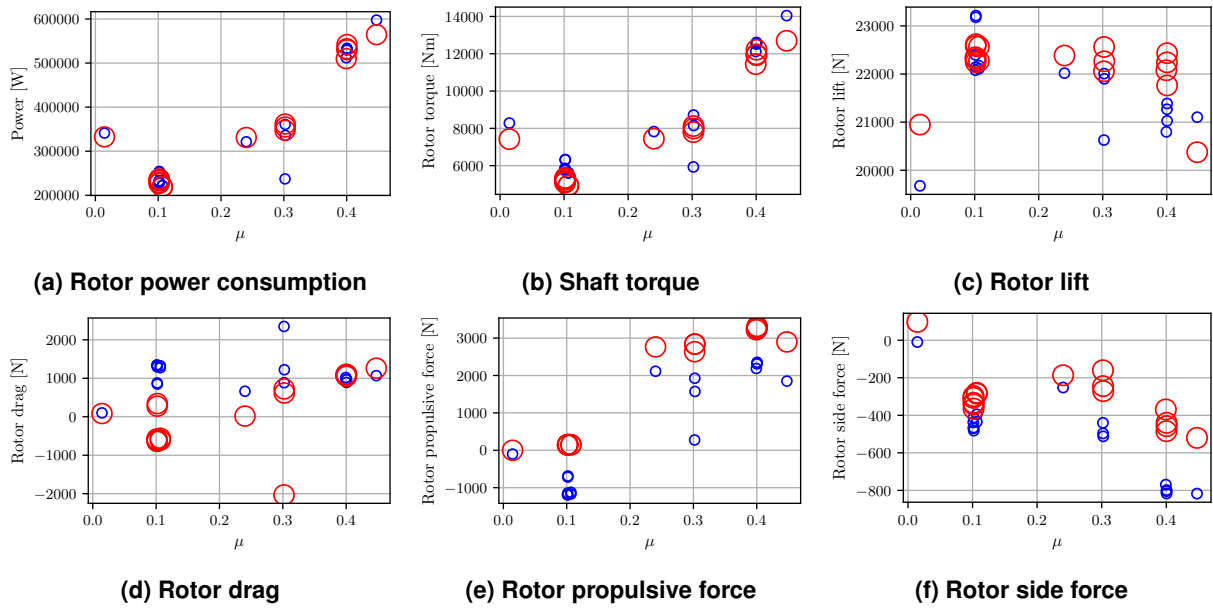


Figure 6: Comparison of Bo 105 rotor trim forces and moments between measurements (Ref. 28) and simulation results. \circ - Simulation \circ - Expt.

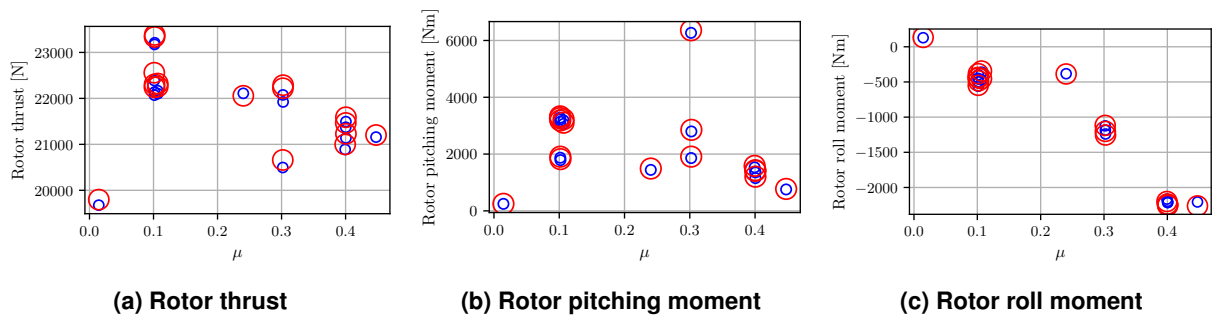
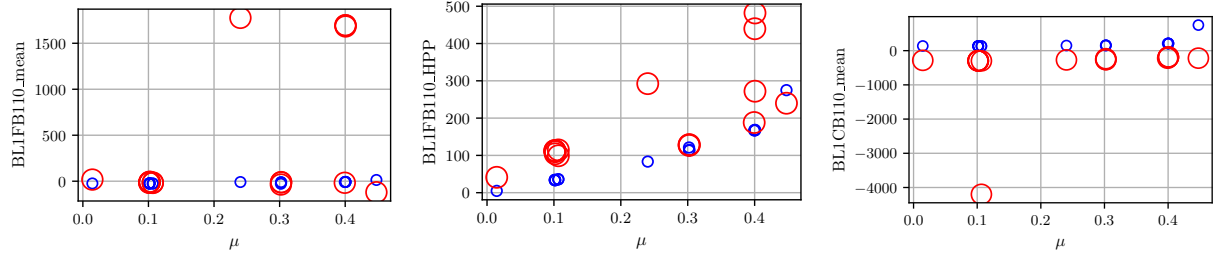
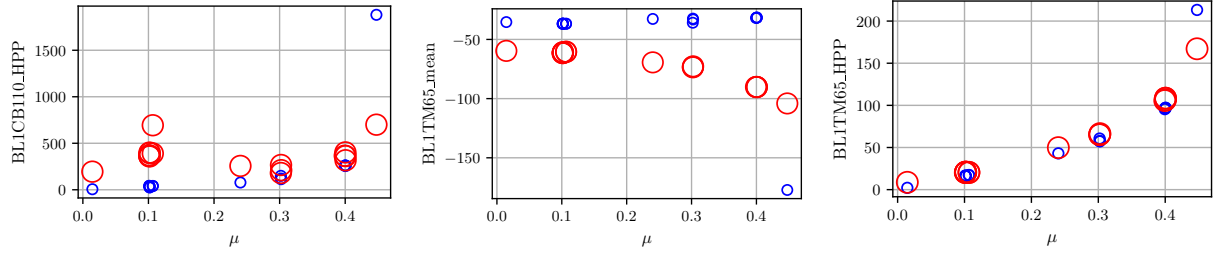


Figure 7: Comparison between the measured rotor thrust and moment used in order to trim the Bo 105 rotor (Ref. 28) and the corresponding results from the trimmed simulation. \circ - Simulation \circ - Expt.



(a) Blade 1 mean flap bending loads at 53.5%R (b) Blade 1 half peak-to-peak flap bending loads at 53.5%R (c) Blade 1 mean chord bending loads at 53.5%R



(d) Blade 1 half peak-to-peak chord bending loads at 53.5%R (e) Blade 1 mean twisting moment at 28.5%R (f) Blade 1 half peak-to-peak torsional moment at 28.5%R

Figure 8: Comparison of Bo 105 rotor blade structural forces and moments between measurements (Ref. 28) and simulation results. \circ - Simulation \bullet - Expt.

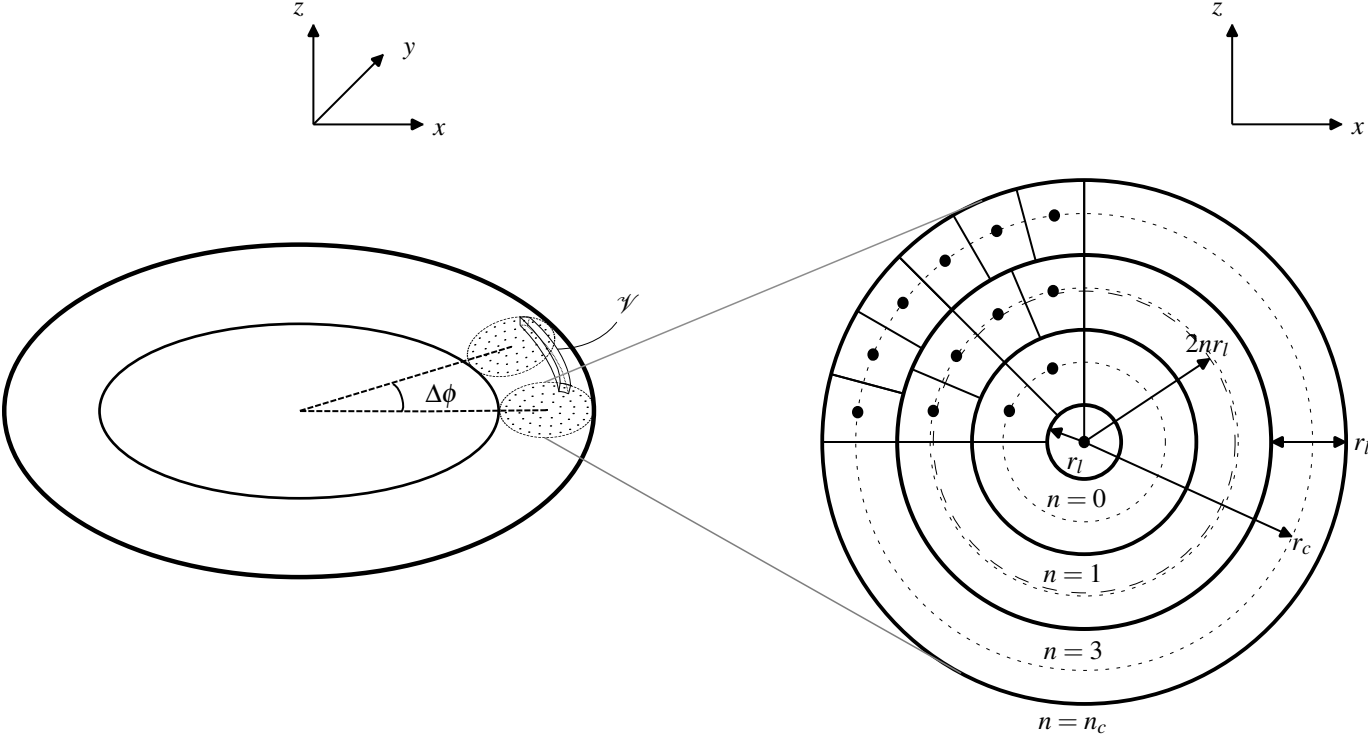


Figure 9: Illustration representing the discretization of the vortex ring of using particles.

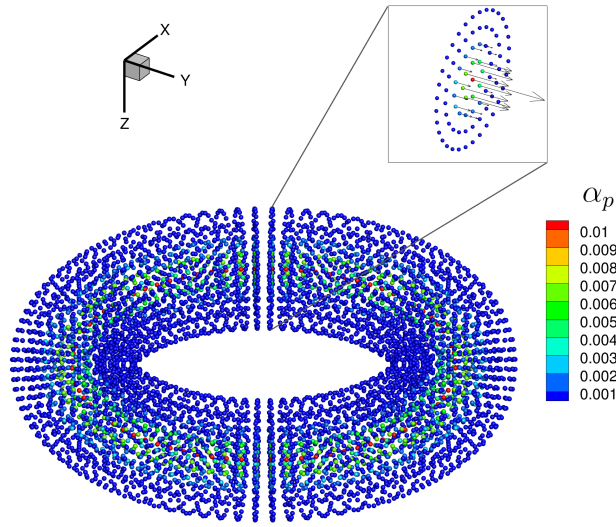
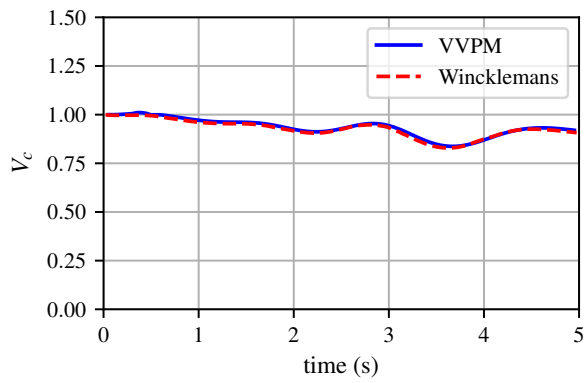


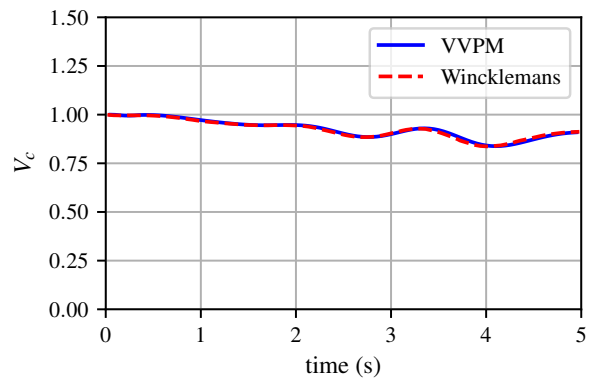
Figure 10: Visualisation of the 4by80 vortex ring.

Layers n_c	$\Delta\phi$	σ [m]	Diagnostic	Current Study	(Ref. 27)	(Ref. 23)	(Ref. 29)
4	4.50°	0.1	$ \mathbf{I} $	3.1655	3.2139	3.1654	3.1654
			$E_{\sigma f}$	1.0168	1.0476	1.0167	1.0167
			E_{σ}	1.0167	1.0475	1.0166	1.0166
			$\mathcal{E}_{\sigma f}$	60.4148	62.3842	60.4121	60.4120
			\mathcal{E}_{σ}	61.4135	61.3464	61.4109	61.4108
			V_c	0.2601	0.2660	0.2496	0.2495
			dE_{σ}/dt	-0.1223	-0.1276	-0.1496	-0.1235
5	3.60°	0.084	$ \mathbf{I} $	3.1785	3.2154	3.1785	3.1731
			$E_{\sigma f}$	1.0137	1.0365	1.0136	1.0103
			E_{σ}	1.0137	1.0364	1.0136	1.0103
			$\mathcal{E}_{\sigma f}$	57.6523	58.9907	57.6503	57.5490
			\mathcal{E}_{σ}	58.3194	58.3052	58.3174	58.3068
			V_c	0.2627	0.2660	0.2510	0.2505
			dE_{σ}/dt	-0.1225	-0.1268	-0.1526	-0.1234
6	3.08°	0.073	$ \mathbf{I} $	3.1865	3.2184	3.1864	3.1731
			$E_{\sigma f}$	1.0121	1.0314	1.0121	1.0103
			E_{σ}	1.0121	1.0314	1.0121	1.0103
			$\mathcal{E}_{\sigma f}$	56.0832	57.1632	56.0819	57.5490
			\mathcal{E}_{σ}	56.6203	56.6137	56.619	58.3068
			V_c	0.2632	0.2662	0.2519	0.2505
			dE_{σ}/dt	-0.1230	-0.1268	-0.1534	-0.1234

Table 5: Comparison of diagnostics of the vortex ring, based on Table 4, across different studies available in literature.



(a) 4by80 vortex ring



(b) 5by100 vortex ring

Figure 11: Comparison of predicted centroid convection velocity for different vortex ring discretizations using the current implementation and results available in Ref. 27.

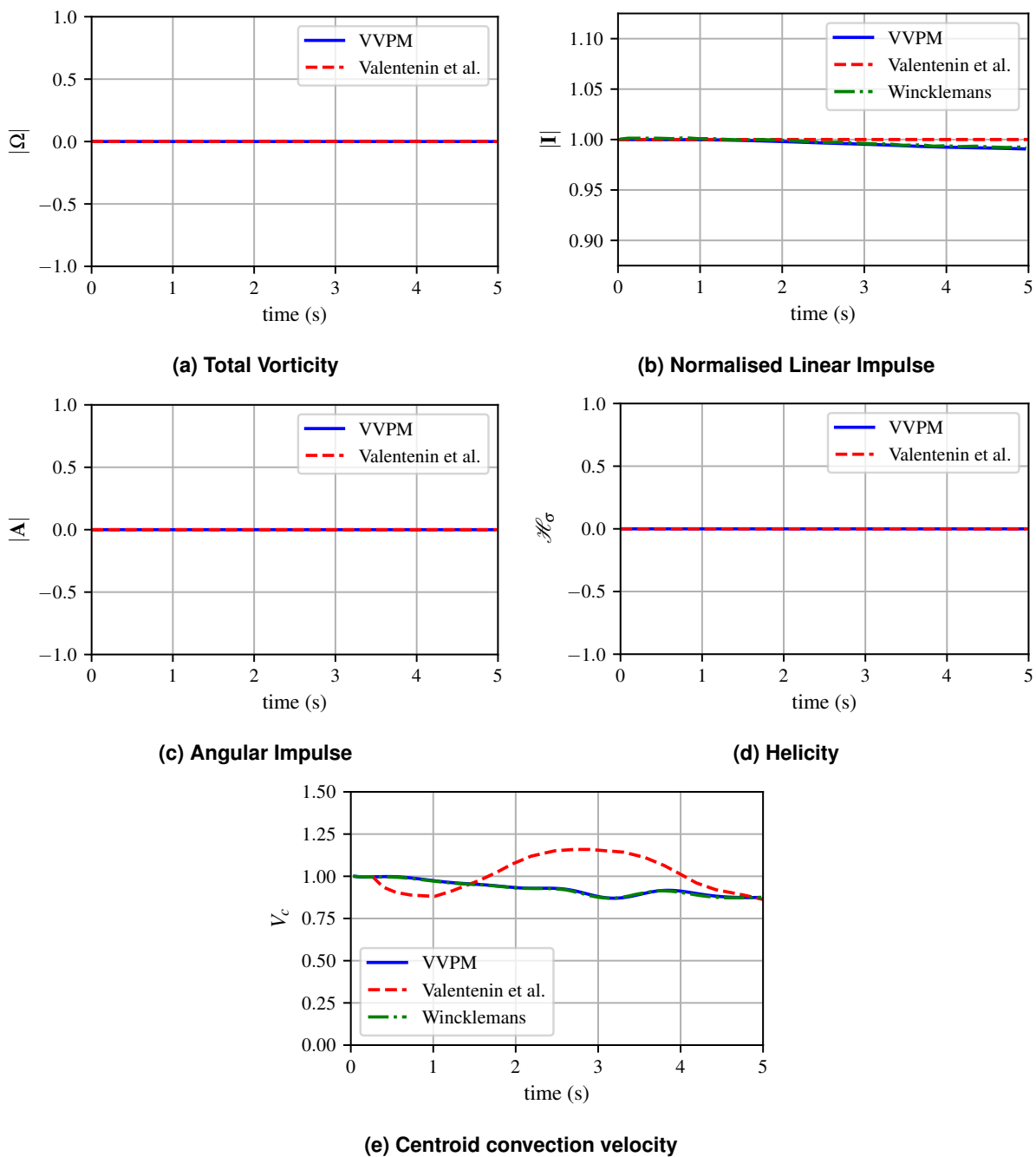
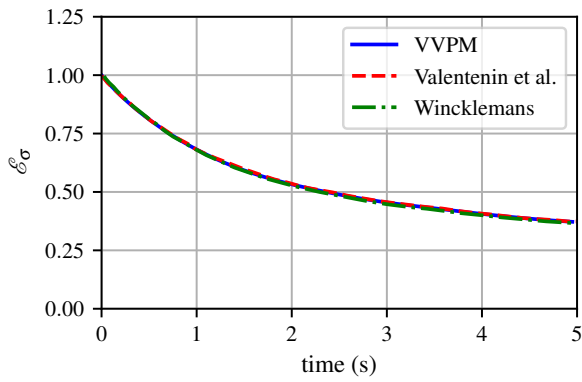
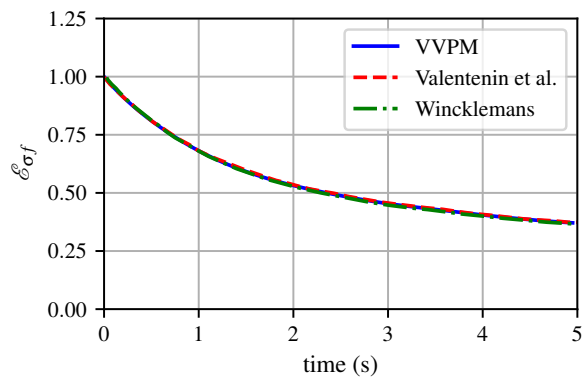


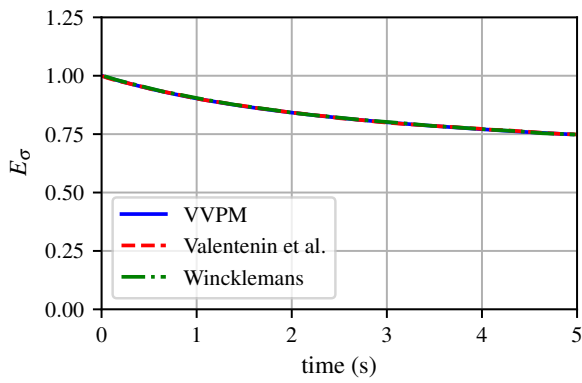
Figure 12: Comparison of predicted linear flowfield diagnostics and convection velocity of 6by117 vortex ring between the current implementation and those available in Refs. 29 and 27.



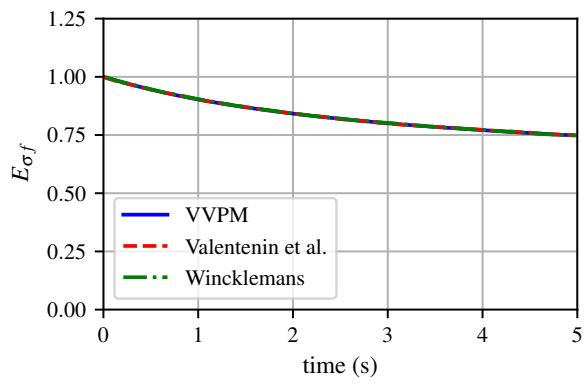
(a) Normalised Enstrophy



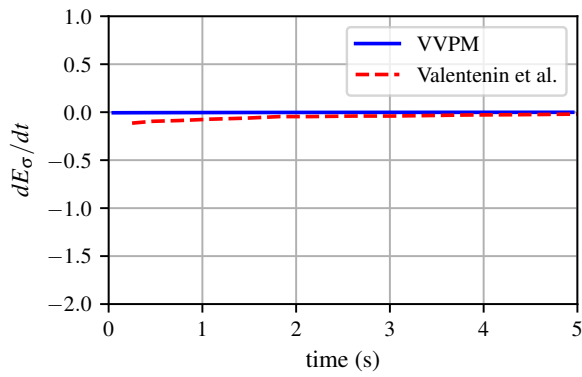
(b) Normalised Enstrophy (div-free)



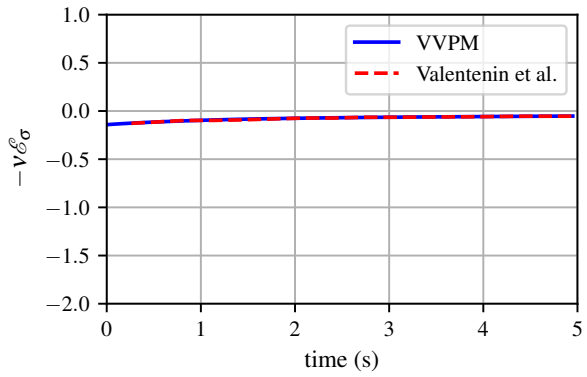
(c) Normalised Kinetic Energy



(d) Normalised Kinetic Energy (div-free)

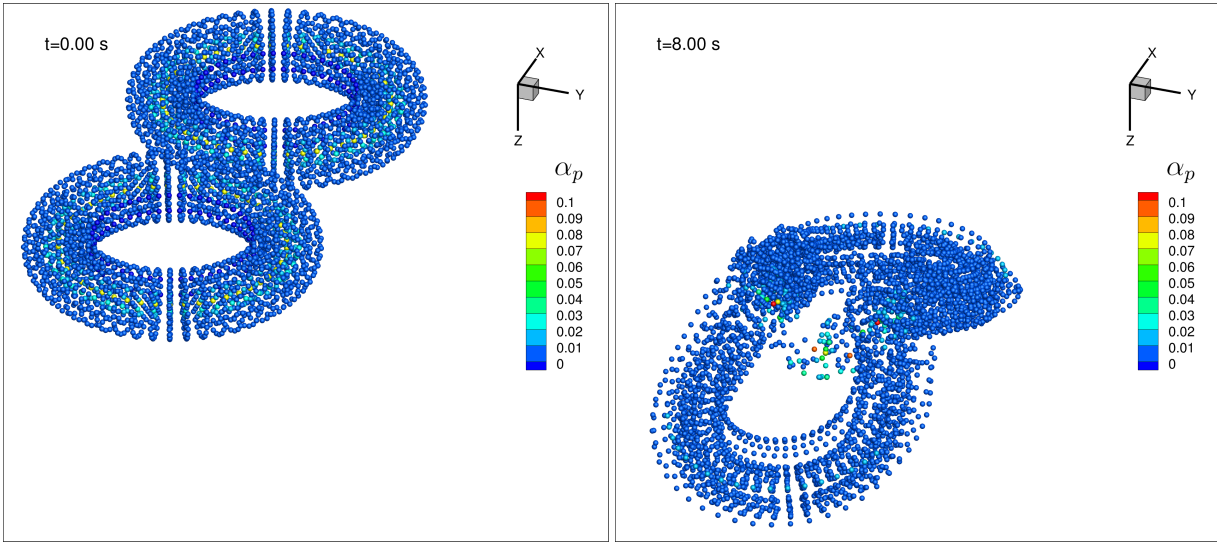


(e) Rate of change of Kinetic Energy



(f) Theoretical kinetic energy decay rate

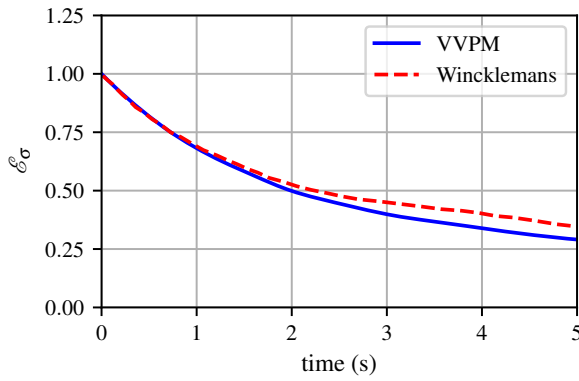
Figure 13: Comparison of predicted quadratic flowfield diagnostics and convection velocity of 6by117 vortex ring between the current implementation and those available in Refs. 29 and 27.



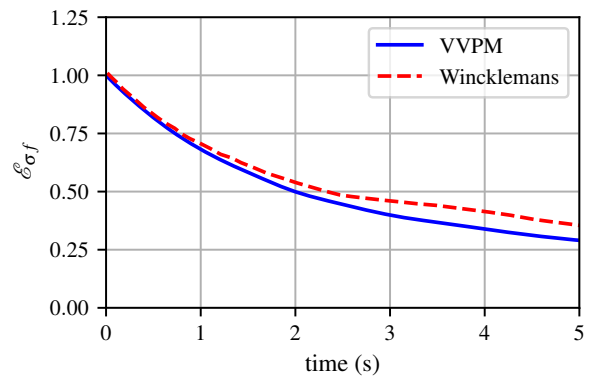
(a) Vortex rings at the beginning of simulation

(b) Vortex rings after fusion

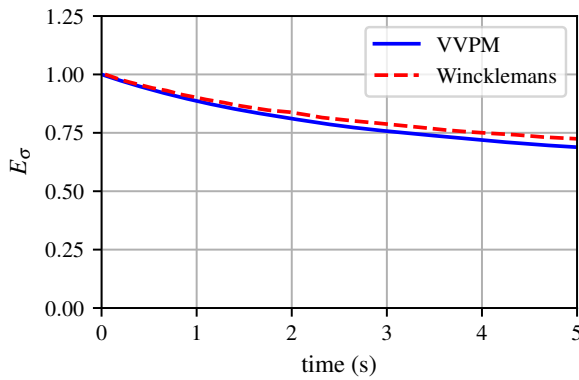
Figure 14: Visualisation of the evolution of fusion between two 3by49 vortex rings.



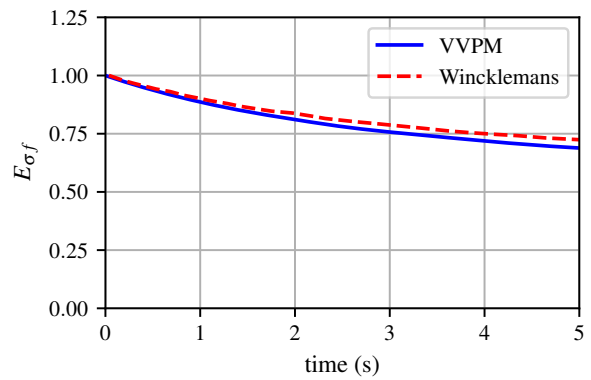
(a) Normalised Enstrophy



(b) Normalised Enstrophy (div-free)

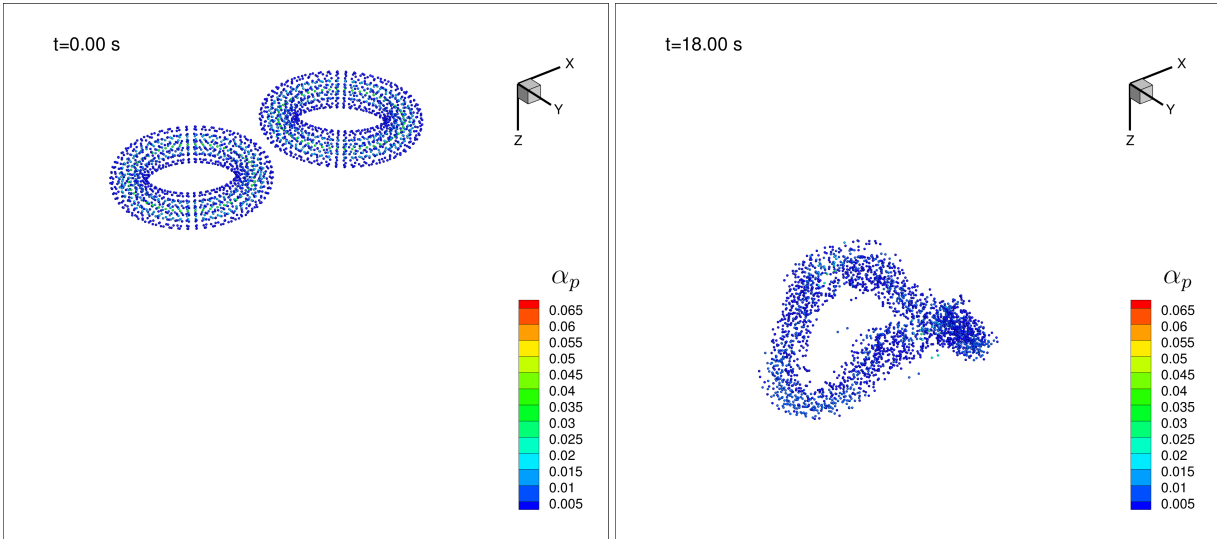


(c) Normalised Kinetic Energy



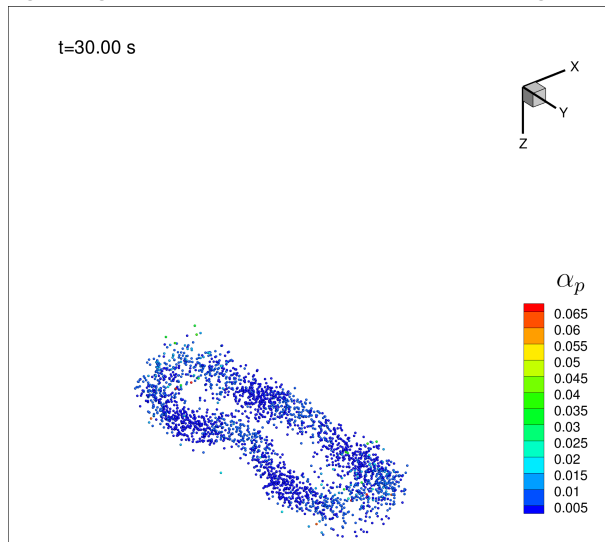
(d) Normalised Kinetic Energy (div-free)

Figure 15: Comparison of predicted flowfield diagnostics during the fusion of two 3by49 vortex rings using the current implementation and that available in Ref. 27.



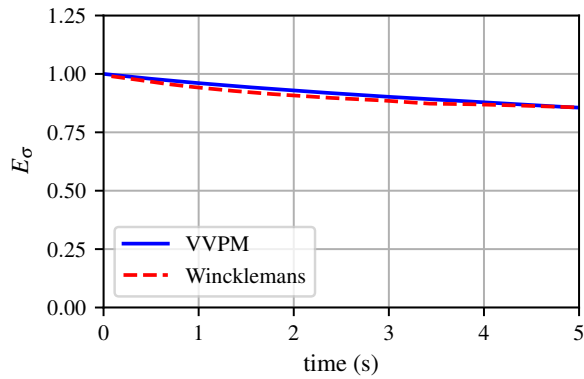
(a) Vortex rings at the beginning of simulation

(b) Vortex rings after fusion has occurred

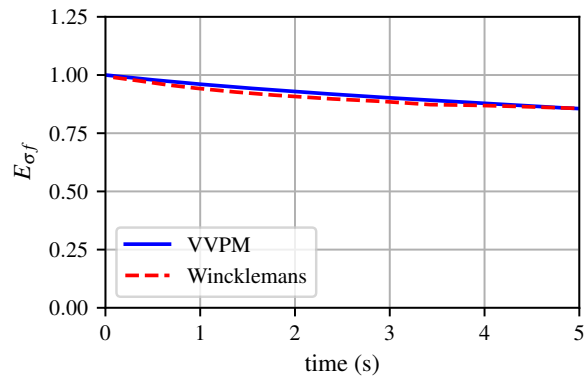


(c) Vortex rings before fission occurs

Figure 16: Visualisation of the evolution of fusion-fission between two 2by52 vortex rings.

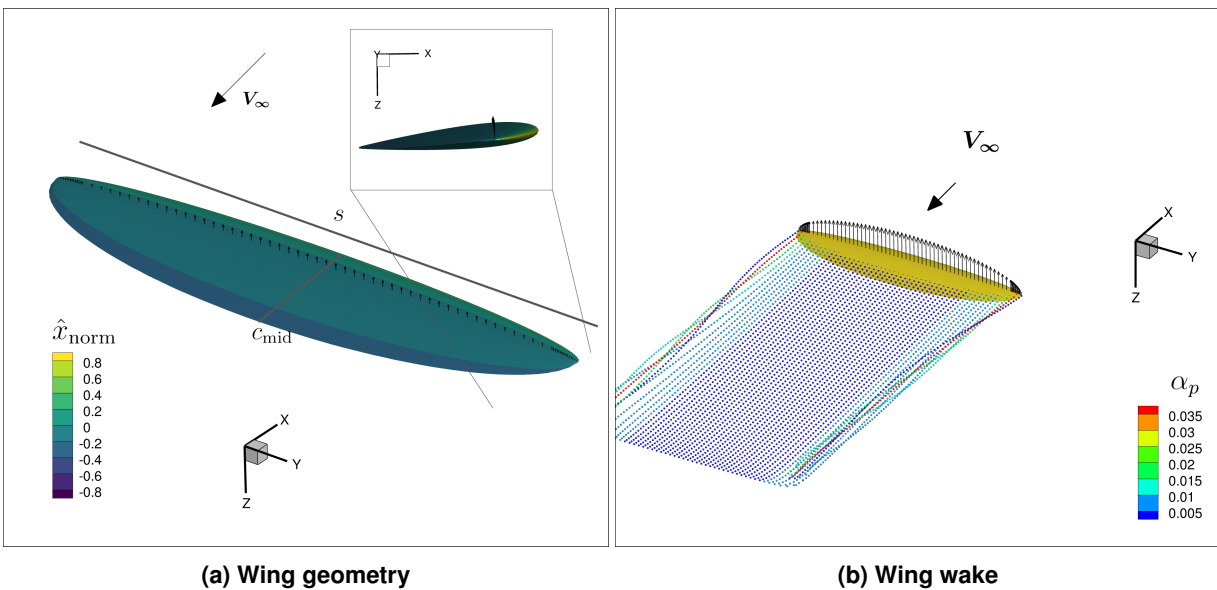


(a) Normalised Kinetic Energy



(b) Normalised Kinetic Energy (div-free)

Figure 17: Comparison of predicted flowfield diagnostics during the fusion-fission of two 2by52 vortex rings using the current implementation and those available in (Ref. 27).



(a) Wing geometry

(b) Wing wake

Figure 18: Schematic of the elliptic wing geometry and the wake generated using Dymore+VVPM framework.

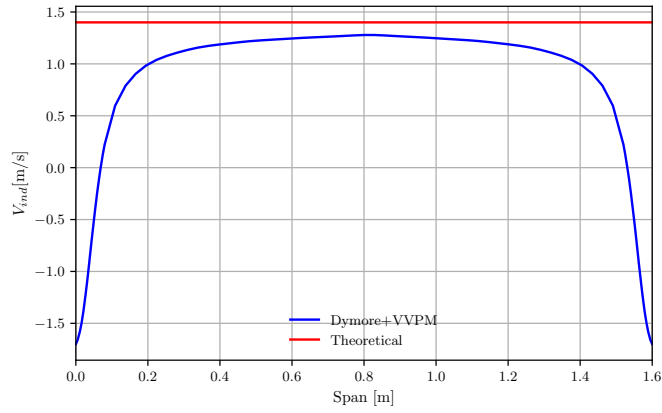


Figure 19: Comparison between the theoretical and the predicted induced velocity due to trailing vortices from an elliptical wing.

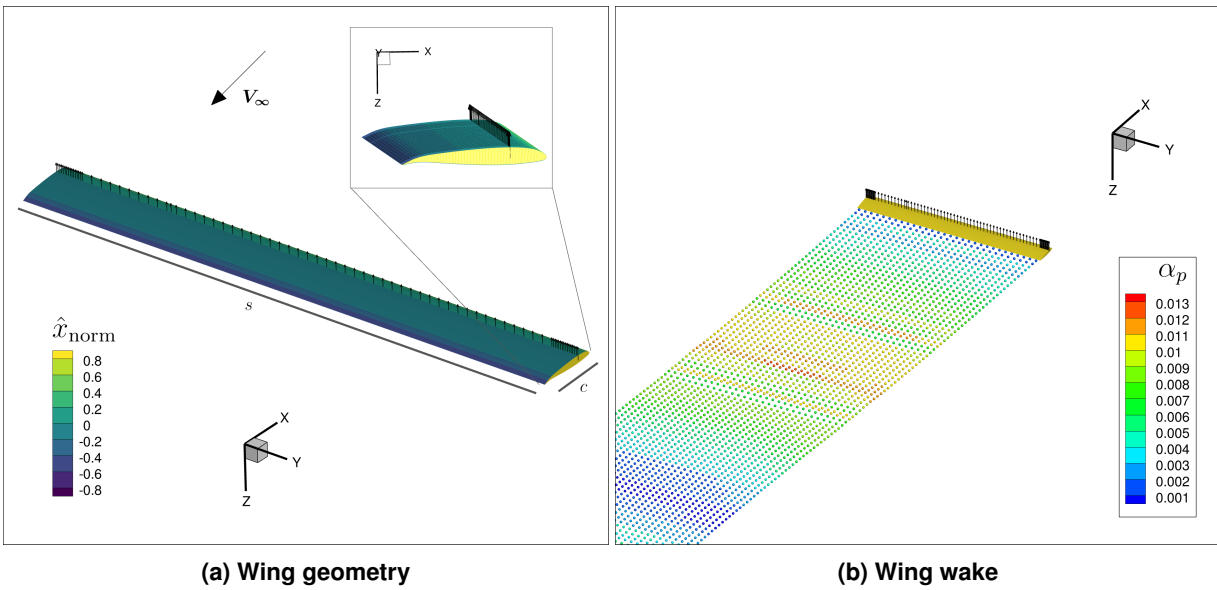
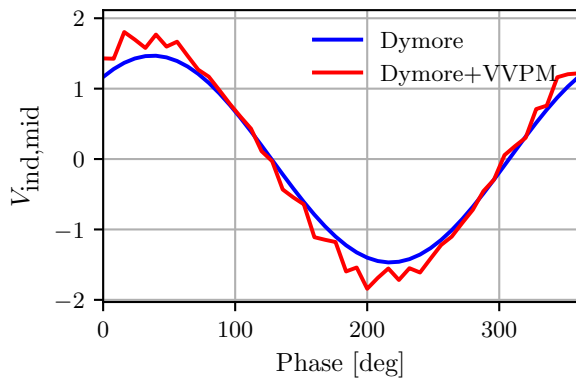
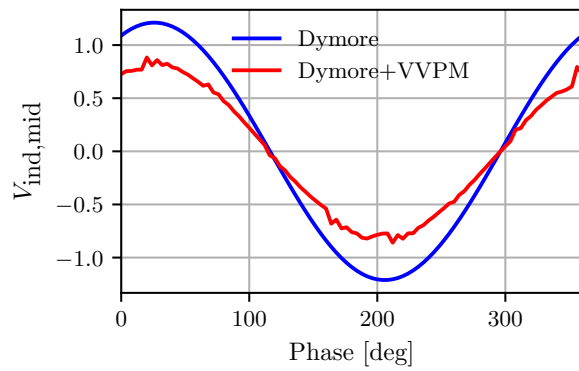


Figure 20: Schematic of the rectangular wing geometry and the wake generated using Dymore+VVPM framework.



(a) Rectangular wing morphing at 10Hz



(b) Rectangular wing pitching at 5Hz

Figure 21: Comparison of unsteady wake induced velocity at the mid-wing section using standalone Dymore model, with 2D unsteady aerodynamic models, and Dymore+VVPM framework.